Enhancing Proton Mobility in Polymer Electrolyte Membranes: Lessons from Molecular Dynamics Simulations

E. Spohr,* P. Commer, and A. A. Kornyshev

Institut für Werkstoffe und Verfahren der Energietechnik (IWV-3) Research Center Jülich, D-52425 Jülich, Germany

Received: January 23, 2002; In Final Form: June 19, 2002

Typical proton-conducting polymer electrolyte membranes (PEM) for fuel cell applications consist of a perfluorinated polymeric backbone and side chains with SO_3H groups. The latter dissociate upon sufficient water uptake into SO_3^- groups on the chains and protons in the aqueous subphase, which percolates through the membrane. We report here systematic molecular dynamics simulations of proton transport through the aqueous subphase of wet PEMs. The simulations utilize a recently developed simplified version (Walbran, A.; Kornyshev, A. A. *J. Chem. Phys*. **2001**, *114*, 10039) of an empirical valence bond (EVB) model, which is designed to describe the structural diffusion during proton transfer in a multiproton environment. The polymer subphase is described as an excluded volume for water, in which pores of a fixed slab-shaped geometry are considered. We study the effects on proton mobility of the charge delocalization inside the SO_3^- groups, of the headgroup density (PEM "equivalent weight"), and of the motion of headgroups and side chains. We analyze the correlation between the proton mobility and the degree of proton confinement in proton-carrying clusters near SO_3^- parent groups. We have found and rationalized the following factors that facilitate the proton transfer: (i) charge delocalization within the SO_3^- groups, (ii) fluctuational motions of the headgroups and side chains, and (iii) water content.

1. Introduction

Perfluorinated membranes are widely used in liquid and gas separation, water electrolysis, electro-organic synthesis, catalysis, electrochemical synthesis, nanoparticle synthesis, and protective clothing. Nowadays, particular attention is drawn to their use in polymer electrolyte fuel cells (PEFC),[1,2] which are the most promising renewable power generators for emission-free vehicles, portable applications, and main or backup power supplies for individual homes (for recent coverage, see ref 3). The polymer electrolyte materials acceptable for direct use in fuel cells are composed of polymer molecules with side chains containing acidic groups.[4−6] In the wet state, these groups dissociate and deliver protons as charge carriers. Requirements on the polymer electrolyte membrane (PEM) in a fuel cell are strict. An "ideal" membrane must be (i) chemically and mechanically stable, with a steady performance in the temperature range of 80−150 °C at a conductivity not lower than 0.1 S cm^{-1} and (ii) impermeable to gases, methanol, and contaminating ions.

The impermeability to methanol is important for direct methanol fuel cells (DMFC), where the fuel is CH_3OH instead of H_2 and permeation of unconsumed methanol from the anode to the cathode leads to significant voltage losses. The best known PEMs, such as Nafion (DuPont), Dow (Dow Chemicals), Gore, and Acipex (Asahi), meet, apart from their current high price, by and large the demands of hydrogen−oxygen fuel cells. Their shortcomings are the large electroosmotic effect (co-transport of water together with the protons) together with a strong dependence of proton conductivity on water content, that, in combination, lead to significant losses at large currents. All these materials are, however, unsuitable for the direct methanol fuel cell, as they are (i) permeable to methanol and (ii) cannot sustain the elevated temperatures at which the catalyst would have consumed all the methanol in the anode compartment, thereby making the issue of methanol permeation unimportant.

Development of new membranes that could meet all these demands is yet a dream that polymer chemists try to bring to reality. It seems clear, however, that fulfilling all the requirements simultaneously may not be possible with a homogeneous membrane. Therefore, polymer engineers develop, for example, membranes with implanted submicron palladium fillers, which are conductive for protons but impermeable to water and methanol.

The requirements of hydrogen PEFCs are somewhat easier to fulfill. Here, the primary tasks are high proton conductance of the membrane over a wide range of water content at a low water mobility. The two goals can hardly be reconciled: typically, faster water diffusion occurs together with faster proton transport. For instance, if the membrane takes up more water, which results in a larger mean pore radius at full saturation, then the proton mobility in the membrane approaches that in bulk water,[1] but the electro-osmotic coefficient increases as well.[7] To find a way to increase the proton mobility at unaltered water transport coefficients is thus a challenging task. However, because the proton mobility can hardly become higher than in bulk water, the task will be to increase the proton mobility at intermediate water content.

For such complex systems as PEMs, computer simulation methods are the theoretical method of choice. Molecular dynamics (MD) simulations in particular allow the calculation of single-particle dynamics (self- or defect diffusion coefficients) or collective dynamics (conductivity). This approach has been used by several groups. The following studies are interesting in the current context. Münch et al.[8] studied proton dynamics in the high-temperature phase of solid $CsHSO_4$ by means of purely classical MD simulations, where the proton was modeled as a simple charged entity, and concluded that proton motion

* Corresponding author. E-mail: e.spohr@fz-juelich.de.

10.1021/jp020209u CCC: $22.00
Published on Web 09/24/2002

inside the crystal was uncorrelated and "liquidlike". More recently, Paddison et al. studied fragments of the Nafion polymer network such as trifluoromethanesulfonic acid[9] and the pendant Nafion side chain[10] by molecular modeling techniques in which they characterized hydrophilic sites by means of a water test molecule; however, these authors did not carry out a full MD simulation with this model. Ennari et al.[11] performed proton transport MD simulations in which they compared the diffusion coefficient of an atomistic model of the hydronium ion with that of a simplified "proton" model, which is a large spherical cation, similar in size to Na^+ or K^+. In that model, the Lennard-Jones parameters are chosen such that the diffusion coefficient of the ion is in agreement with the overall proton diffusion coefficient in water; the model does not, however, employ the relay mechanism of proton transfer in aqueous environments. Vishnyakov and Neimark investigated the solvation of the Na^+ form of Nafion oligomers in neat water and neat methanol by MD[12] and observed differences in chain configurations. In a study of the K^+ form in an equimolar methanol−water mixture,[13] the same authors observed preferential solvation of the skeleton by methanol but no preference for solvation of the side chains. More recently they attempted a study of microphase segregation between water and Nafion oligomers.[14] They observed water clusters with a rather wide size distribution, which appeared not to form a continuous hydrophilic phase, and the forming and breaking of temporary bridges between the clusters. All the cited studies either do not investigate proton diffusion directly or do not take into account the known cooperative aspects of proton transport in aqueous phases.

Proton mobility in water is a long-standing problem (see, for example, the conceptual reviews[15,16]) that has recently been revisited in a number of publications. A series of Car−Parrinello ab initio simulations on the transport of the proton in bulk water and in water clusters[17−21] revealed that the proton state in the liquid indeed fluctuates between more localized hydronium ion-like states (Eigen ion) and more delocalized $H_5O_2^+$-like states (Zundel ions). The proton transport is associated with the forming and breaking of hydrogen bonds in the neighborhood of the proton position. Empirical valence bond (EVB) models were used in a series of simulations[22−29] of proton clusters and protons. By construction, these models incorporate the ability of the proton to undergo a Grotthus-like hopping, by which it is transferred from an H_3O^+ ion to a neighboring water molecule. Mixed quantum/classical dynamics of proton migration in water[30,31] treated only the so-called proton-transfer coordinate quantum mechanically. By construction, the computational effort to handle more than one proton with these models increases exponentially and is thus not suitable for the concentrated protonic solution present in the nanopores of a Nafion-like PEM.

Walbran and Kornyshev[32] modified existing EVB models in order to achieve a local description of the proton-transferring complex with a basis of only two valence bond states. This approach allows the simulation of concentrated solutions. The present paper investigates proton transport in concentrated aqueous proton solutions in slab pores on the basis of this model. The slab pores serve as models for nanopores in Nafion-like PEMs and are modeled in a variety of different ways (see section 4). By comparing the simulation results with existing theoretical concepts,[33−35] we will try to rationalize the mechanism of the elementary act of proton transfer in the membrane interior and reveal the key factors that influence the rate of proton transport.

It should be noted, however, that the model in ref 32 has several drawbacks. It does not describe the delocalized nature of the proton as adequately as the more elaborate EVB models. Although it predicts the correct value for the activation energy of proton diffusion, the absolute value of the mobility is only half the experimental value. Next, water diffusion is higher than in bulk water, probably because of the introduction of a (fast) polarizability term that allows the proton transport to speed up into the originally nonpolarizable Toukan−Rahman model (see ref 32 for details). Nevertheless, there is currently no alternative model that (i) has the essential physics of proton transport built in and (ii) can be handled computationally for the required system size and proton concentration. Consequently, because the model does describe the interplay between the Eigen and Zundel states and the resulting charge-transfer dynamics, it is useful for the analysis of the effect of the membrane environment on proton transport in intramembrane water channels.

The organization of this paper is as follows. In the next two sections, the current understanding of membrane properties and of the proton-transport mechanism in aqueous systems is outlined. We then discuss the slab models and simulation techniques. The subsequent section contains the description of simulation results. It is followed by a discussion where we summarize the main trends emerging from the simulation data.

2. Membrane Structure and Phase Segregation in PEMs

The unique properties of PEMs are related to their complex nanostructure. It is well documented that, when exposed to water or other hydrophilic solvents, the polymer electrolyte undergoes a nanoscale segregation into two subphases.[14] The hydrophobic subphase is formed by the organic backbone. The hydrophilic subphase is formed by largely immobile negative charges of SO_3^- groups on the side chains, mobile countercations, and absorbed water. When countercations are protons, the hydrophilic phase is able to conduct them, and when this phase spans (percolates) through the whole polymer, the membrane becomes a good proton conductor. Percolation may have dynamic character. Indeed, in poorly performing membranes, water could be inhomogeneously distributed, forming large water clusters at the expense of water-free domains; transport between the clusters may be a result of fluctuating short-lived bridges.[14]

The proton mobility in the hydrophilic phase was never observed to be higher than in pure water, but the density of donated protons is, like in concentrated acids, orders of magnitude higher, which leads to appreciable proton conductivity. Whereas this qualitative picture is more or less commonly accepted, there are controversial opinions concerning the morphology of the microphase segregation. The structure was studied by small-angle X-ray and neutron[36−39] scattering. The measurements are known to be poorly reproducible for identically labeled samples ("batch" dependence). Furthermore, a hysteresis of properties of the same sample with hydration/dehydration cycles is typically observed. This indicates that the membrane structure is usually not an equilibrium structure. In this sense, the proton-conducting membrane is like a living organism: it needs water to function, and its structure is not in the ground state.

Nevertheless, experiments can give valuable hints concerning the size and shape of the characteristic structural units (such as inverted spherical micelles, cylinders, lamellas, and the like) and the basic principles governing their spatial distribution. The existing data[36−39] favor a view that different membranes range between (i) a heterogeneous porous material amenable to swelling, similar to but weaker than a sponge and (ii) a homogeneous material such as a concentrated solution of a polyelectrolyte. The former view appears to be more likely

because homogeneous materials are not expected to show such a hysteresis. Homogeneous solutions of strong acids possess a reproducible local chemical structure and do not show any hysteresis with variations of the concentration. In view of the history dependence of properties and of the phase segregation, one may regard the membrane as a soft "glassy" nonequilibrium composite with water as one of its components.

Conducting virtual computer experiments (such as Monte Carlo and molecular dynamics simulations), which simulate the membrane structure as the result of self-assembly, is a thankless task that is hardly achievable with existing top-level computational facilities (for first attempts, see, for example, refs 12 and 14). Indeed, molecular simulations of microphase segregation require very large model systems (considerably larger than the characteristic size of the hydrophilic aggregates), which makes the simulation of polyelectrolyte structures a computational impossibility. Furthermore, simulations of polymers in general are nontrivial and often involve a difficult choice between force-field accuracy, simulation length, and system size. The existence of metastable domains of nonequilibrium structures in a real polymer membrane, as indicated by the strong dependence of membrane performance on pretreatment, poses a severe ergodicity problem for simulations. We therefore chose not to follow this route but instead followed simulated proton transport in representative water-filled pores of a given structure. In this paper, we confine ourselves to slab pores.

One may ask, what can we learn from it? Indeed, at high electrical currents, the channel structure itself may depend on the current; in addition, the water content may influence the morphology of the water-filled regions. Furthermore, the local water content may vary along the sample as a consequence of the electrical current passage.[40] The answer is, however, simple: if this approach could shed light on prospective polymer structures that facilitate proton mobility with no significant effect on water mobility, our efforts would be justified. This consideration is the basis of the approach used in this paper.

3. Theoretical Views of Proton Transport in Aqueous Systems and Hydrated Membranes

Water is a "democratic" environment for protons. A donated excess proton becomes indistinguishable from other protons, but it gives birth to charged clusters in water. These are, first of all, the bare hydronium ion H_3O^+ with three *equivalent* protons, then a *hydrated* hydronium ion with three strongly bound water molecules (which is called the Eigen cluster $H_9O_4^+$ [41]), and also the symmetric $H_5O_2^+$ complex in which a proton is shared between two water molecules (called the Zundel ion[42]). Many intermediate or more-complex states of the "hydrated proton", $H^+(H_2O)_n$, can also be envisaged. However, the mentioned states of the proton seem to be the basic three units observed spectroscopically[43] and in simulations.[26,32,44,45] All clusters have a finite lifetime and transform into each other during charge transport. Subject to the relative abundance of these three basic states, proton transfer occurs via different pathways.[16]

The most straightforward transport mechanism for any proton of an H_3O^+ donor is the hopping to a neighboring water molecule. For this to happen, a neighboring water molecule must approach one of the protons in the H_3O^+ ion in such a way that an intermediate adduct similar to the Zundel complex is formed, where this proton is in the bridge position. From this state, there are two possible pathways in which $H_5O_2^+$ dissociates into a hydronium ion and a water molecule. If there is further charge transfer, then a new H_3O^+ acceptor state is formed, and the water molecule of the former donor must fluctuate out of the $H_5O_2^+$ state. In the back reaction, the charge moves back to the original hydronium ion and the "attacking" water will again move out of the $H_5O_2^+$ adduct.

This also carries over to mechanisms based on the $H_9O_4^+$ cluster. Here, charge transfer is triggered by shifting the charge center from the central H_3O^+ toward one of the hydration water molecules that serves as an acceptor. The other two water molecules from the original Eigen complex keep hydrating the newly formed Zundel ion.

A second pathway is the structural diffusion of $H_5O_2^+$. An attacking water molecule next to such a cluster fluctuates into a configuration where the proton charge is delocalized over more than just two molecules. Then, a new $H_5O_2^+$ cluster is formed. Subsequent fluctuations may move one of the original water molecules out of the proton cluster. In effect, the charge is moved to a new position; the back reaction, namely, that the attacking water molecule leaves the cluster, is also possible, which leads back to the original Zundel ion. The formation of the new Zundel ion may proceed along any of the four external protons of the original $H_5O_2^+$ cluster.

When both Zundel and Eigen ions account for a sizable fraction of proton states (as seems to be the case on the basis of simulations), then these two proton-transport pathways become equivalent in the sense that proton transport arises from a chain of consecutive Eigen-to-Zundel and Zundel-to-Eigen transitions.

Last but not least, the H_3O^+ ion can drift classically as a whole, like a hydrated alkali ion. However, this is only one of the contributions to the proton transport, and is certainly not the dominating contribution in bulk water. This mechanism is obscured by the possibility of the relay transport mechanism via the hydrated proton clusters.

In all these elementary processes, the key step is associated with the making or breaking of a hydrogen bond, which allows a water molecule to either attach itself to the cluster or leave the cluster. This preorganization of the pertinent water molecules make the proton transfer itself virtually barrierless, and it determines the time scale of the elementary act of structural diffusion. For the model to be used in the present work,[32] which reproduces the essential features of structural diffusion,[46] this time is several picoseconds.

Note that although this microscopic view emerged recently from breakthrough quantum molecular dynamics simulations,[44] researchers had been developing this picture of proton transfer in water for many years (for historical overviews, see refs 15, 16, and 47 and the introductory parts of several recent original papers[26,44,32,45]).

Which modifications of the proton-transport mechanism do we expect in the membrane environment? First, near the pore surface (i.e., near the SO_3^- groups), the structure of water may be significantly different than in the bulk water. Dielectric relaxation signals from narrow water channels in membranes at low water uptake suggest that water is pretty much "frozen" in comparison to the bulk phase.[48] As a consequence, higher barriers for molecular preorganization are expected, resulting in higher effective activation energies for proton transfer. The formation of new structures could be accompanied by significant modifications of the nature and lifetimes of different proton-transfer clusters.

Furthermore, proton transfer near an array of SO_3^- ionic groups never proceeds between equivalent states because the typical distances between the SO_3^- groups (0.7−1 nm for the relevant materials) are too large for a single transfer. Thus, a

Coulomb barrier exists, which the transferring proton has to overcome. This Coulomb barrier is the energetic cost of the proton leaving the mother sulfonate group.[49] In ref 50, it was shown that this work term is smaller the denser the array of SO_3^- groups.

Yet another mechanism might also be possible: the side chains carrying the SO_3^- groups can move ("bow") toward each other to facilitate symmetric proton transfer with zero reaction free energy. The energetic expense for this process will be the work to bring two charged groups together up to distances that are amenable for a group-to-group elementary act of proton transfer. This will probably contribute a similar amount of activation energy as that needed for proton liberation from the SO_3^- mother group. However, the overall nonconcerted fluctuations of the side chains will smear the in-plane and out-of-plain Coulomb barriers, thereby reducing the effective activation energy for the surface conductivity process.

According to the mean-field theory of ref 49, there is a radial distribution of proton density in the pore with the minimum in the middle of the pore. If the pore is large, then there is a large amount of bulklike water. The width of the diffuse double layer determines the number of protons in the central bulklike region of the pore. These protons will show the highest mobility. Thus, the conductance of the pore will approach that of bulk water because of the low activation energy of proton mobility in bulk water. In narrow pores, there is no "bulk", and conductance can be expected to occur predominantly via the "surface mechanism".

The goal of this study is to explore how the side chains' charge distribution, flexibility, and fluctuations affect the proton transfer in representative membrane pores in order to shine light on possible proton-mobility reserves at moderate and low water content, which can be exploited by suitable membrane architecture.

4. Simulation Models and Methods

With this strategy in mind, one may consider proton transport inside pores with model geometries such as slabs, cylinders, and spherical cavities. In the current study, we confine ourselves to slablike pores of fixed width. The chemical details of the Nafion side-chain structure are described in several different ways; the Nafion main chain is replaced by the solid walls of the slab.

We use the polarizable empirical valence bond (EVB) model for water and protons that has been described in ref 32. All potential parameters are exactly as shown there. The model implements the Grotthus-type proton-transfer mechanism into a classical MD simulation. This model yields an activation energy of 0.11 eV for proton diffusion, in excellent agreement with experiment.[32] The caveats of this model (insufficiently high proton mobility and water that is too lively) have been discussed above and in ref 32. All in all, this model implements the relay transport mechanism together with the classical H_3O^+ motion. Because of the localized two-state representation of the EVB states, the model is suitable for the simulation of the multiproton environments in PEM pores.

In a typical simulation, several hundred water molecules and a few protons are confined in a slab of width between 23 and 25 Å. The confinement is realized via an oxygen-wall potential of the 12−6 LJ type

$$V_{\mathrm{O-wall}} = 4\epsilon\left[\left(\frac{\sigma}{z - z_0}\right)^{12} - \left(\frac{\sigma}{z - z_0}\right)^{6}\right] \qquad (1)$$

with $\epsilon = 95.94 \times 10^{-23}$ J and $\sigma = 3.223$ Å. This corresponds to a well depth of $0.2kT$ at $T = 298.15$ K (with the Boltzmann constant k and the temperature T). z_0 is the position of the wall, which is given for each simulation in Table 1. Hydrogen atoms do not interact with the wall. It should be noted that the precise form of the wall potential is of little importance because its well depth is rather shallow and its primary purpose is to produce the excluded volume due to the polymer backbones.

TABLE 1: Simulation Parameters[a]

run	n_w/n^+	n^+	z_0/Å	t_{sim}/ps	$D_\sigma/10^{-5}$ cm^2 s^{-1}	motion	model
I	13.5:1	16	11.5	690	4.9(±0.2)	−	homogeneous charge
II	27:1	8	12.5	715	0.06(±0.1)	−	point charges
III	13.5:1	16	11.6	665	0.04(±0.1)	−	point charges
IV	27:1	8	11.52	750	2.3(±0.2)	−	SO_3^- groups
V	13.5:1	16	11.52	720	0.6(±0.1)	−	SO_3^- groups
VI	13.5:1	16	11.52	530	1.9(±0.2)	−	SO_3^- groups with charges × 0.5
VII	27:1	8	11.52	990	3.6(±0.3)	+	tethered SO_3^- groups
VIII	13.5:1	16	11.52	550	1.7(±0.2)	+	tethered SO_3^- groups
IX	19.1:1	80	11.52	115	3.4(±0.4)	+	flexible side chains

[a] n_w/n^+ is the oxygen/proton ratio, D_σ is the proton diffusion coefficient (see text), $\pm z_0$ are the wall positions, and t_{sim} is the total simulation time. "Motion" indicates whether the positions of the sulfonate groups can move or whether they are fixed. The proton diffusion coefficient in bulk water at room temperature is $D = 4.7 \times 10^{-5}$ cm^2 s^{-1} with this model.[32]

This wall potential, serving as a crude model for the main chain, is augmented by a more-or-less realistic description of the side chains. For each proton in the aqueous phase, there is one countercharge in the system. Different side-chain models differ in the way that this countercharge is distributed and in how the excluded-volume effects of the side chains are accounted for. On purpose, we study different electrostatic, structural, and dynamical features of the side chain separately. The following representations have been chosen in order of increasing complexity:

- No chemical detail. Both slab surfaces contain one-half of the negative countercharge homogeneously distributed over the surface (run I in Table 1). Because both slab surfaces are negatively charged, this case is equivalent to the absence of electrostatic forces acting on charged particles from the boundaries.
- Static point charges. One-half of the point charges are distributed on a regular quadratic grid (as the simplest approach to incorporating a characteristic distance between countercharges) on each slab wall, located at $\pm z_0$. This is done for two different surface-charge densities. The distance between nearest point charges is 9.3 Å (run II) and 6.6 Å (run III).
- Static SO_3^- groups. Lennard-Jones parameters are defined in Table 2. For simplicity, the SO_3^- groups have been made planar (i.e., the O−S−O angle was chosen to be constant at 120°). One-half of the sulfonate groups are set on a regular quadratic grid on each slab wall (at $\pm z_0$). Again, this is done for two different surface-charge densities. The sulfur−sulfur distances between nearest groups are 9.3 Å (run IV) and 6.6 Å (run V).
- The role of partial delocalization of the negative charge along the side chain (a likely electronic effect in perfluorinated Nafion) has been explored in run VI. Here the charges on the S and O atoms are only half their normal values. Otherwise, run VI is identical to run V.
- In runs VII and VIII, the role of headgroup motion is investigated. The sulfur atoms of the sulfonate groups are

TABLE 2: Force-Field Parameters for Simulation Run IX[a]

Lennard-Jones Parameters and Partial Charges q: $V = 4\epsilon[(\sigma/r)^{12} - (\sigma/r)^6]$

	ϵ/kJ mol^{-1}	σ/Å	q/e
C	0.3981	3.473	0.00
F	0.3035	3.093	0.00
O_e	0.7117	3.070	0.00
S	1.0465	3.550	1.19
O_s	0.8372	3.150	−0.73

Stretch Parameters: $V = {}^1/_2k(r - r_0)^2$

	k/kJ mol^{-1} Å^{-2}	r_0/Å
C−C	2928.8	1.54
C−O_e	2928.8	1.54
C−F	2928.8	1.37
C−S	2928.8	1.80
S−O_s	2928.8	1.49

Bend Parameters: $V = {}^1/_2k_\alpha(\cos\alpha - \cos\alpha_0)^2$

	k_α/kJ mol^{-1} rad^{-2}	α_0/deg
C−C−C	471.45	109.60
C−C−F	472.04	109.70
F−C−F	470.70	109.47
S−C−C	490.91	112.60
S−C−F	478.15	110.70
O_s−S−C	456.31	106.75
O_s−S−O_s	509.36	115.00
O_e−C−C	470.70	109.47
C−O_e−C	470.70	109.47
O_e−C−F	470.70	109.47

[a] All torsion terms: $V = {}^1/_2k_\phi\{1 - \cos[3(\phi - \pi)]\}$, $k_\phi = 0.9297$ kJ mol^{-1} rad^{-2}.

tethered via a harmonic interaction of the form

$$V_{\text{tether}}(r) = \frac{1}{2}k_t(\vec{r}_0 - \vec{r}_0)^2 \qquad (2)$$

where $\vec{r}_0$ is the equilibrium position of the sulfur atom on the same quadratic grid as in runs IV and V. The tether force constant $k_t = 828 \times 10^{-23}$ J/Å^2 corresponds to the thermal energy kT at room temperature for a displacement of 1 Å from the equilibrium position. In addition to the tether potential, the SO_3^- groups are confined to the planes at $\pm z_0$.

• A full molecular model of a Nafion side chain has been used in run IX. A Nafion 117 side chain is depicted in Figure 1. In this run, those ether oxygen atoms that connect to the main chain are constrained to move only on a plane that is set 1 Å beyond the wall (at $\pm z_0$). With the exception of this single constraint, the side chains are completely flexible. Specifically, they can undergo conformational changes. The interaction parameters for the side chains are based on the Dreiding force field[51] and are chosen to agree largely with the Nafion model of Vishnyakov and Neimark.[13] The standard Lorentz−Berthelot combination rules have been applied for Lennard-Jones interactions.

This force field is a combination of intermolecular electrostatic and (12−6) Lennard-Jones terms and intramolecular stretch, bend, and torsional degrees of freedom. The parameters are collected in Table 2. It should be noted that several parameters such as the partial charges have been chosen quite freely because producing an accurate description of a particular membrane material was not our intention. We believe that the details of the force-field parameters are not essential for the interpretation of our results because the side chains are not fully mobile and the simulations do not last long enough to allow for self-organization of the side chains other than simple clustering. To allow for comparison with the simpler models, we have set all partial charges on ether oxygen atoms O_e, carbon, and fluorine atoms to zero (not as in the original model of ref 13) so that the negative charge is located entirely on the headgroup, analogous to the model used in runs IV, V, VII, and VIII.

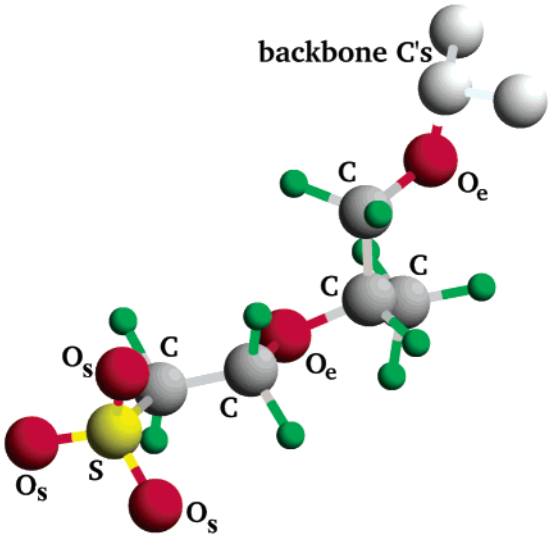

Figure 1. Sketch of the Nafion side chain used in run IX together with definitions of atom types.

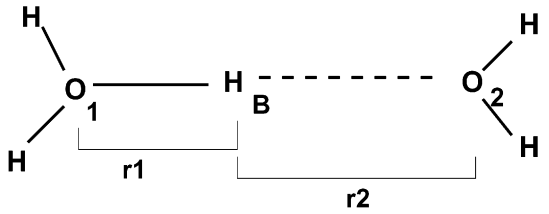

Figure 2. Schematic drawing of the basic EVB (Zundel) complex.

After extensive equilibration over periods between 50 and 150 ps, all simulations were run at 298.15 K over the simulation time specified in Table 1. The Berendsen thermostat[52] was used with a time constant of 1 ps to maintain the average temperature.

5. Simulation Results

5.1. Distributions of Proton States. In the EVB model of ref 32, the excess proton is delocalized between two water molecules (i.e., there are only two zeroth-order EVB states). The Eigen ion, where the proton is localized on one water molecule, is a pure zeroth-order valence bond state. The symmetric Zundel ion, where the proton is shared symmetrically between two water molecules, is the symmetric linear combination of both zeroth-order EVB states. Figure 2 shows, as the most general case of the model, the asymmetric Zundel complex $H_5O_2^+$. The instantaneous state of the proton can be characterized by the proton-transfer coordinate $q = r_1 - r_2$, where $r_1 = |\vec{r}_{O_1} - \vec{r}_{H_B}|$ and $r_2 = |\vec{r}_{O_2} - \vec{r}_{H_B}|$ are, respectively, the smaller and the larger distance between the central bridging (transferring) proton H_B and the oxygen atoms of the EVB complex. With this definition, the symmetric Zundel state corresponds to $q = 0$, whereas large negative values of q ($q < 0.5$ Å according to the model parametrization[32]) correspond to a localized proton in the Eigen state. Note that, because of the definition of r_1 and r_2 as the smaller and the larger OH distance, respectively, only values of $q \leq 0$ can occur.

The distribution of proton states is shown in Figure 3 for the nine simulations I through IX. Our first observation is that the

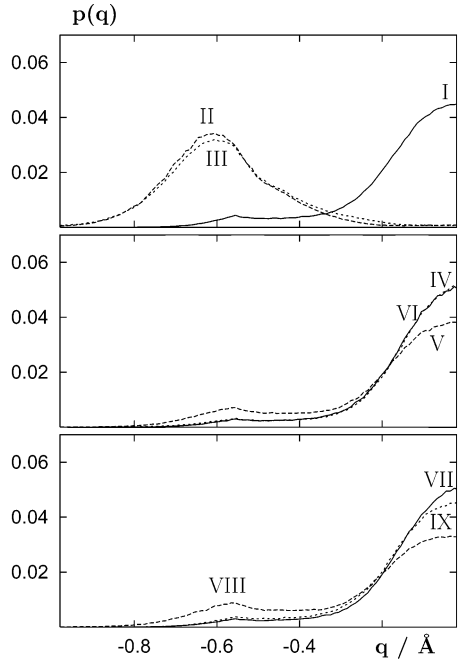

Figure 3. Distribution of the proton-transfer coordinate $q = r_1 - r_2$ (see Figure 2). The region $q \approx -0.5$ corresponds to Eigen ions, and the region $q \approx 0$ corresponds to symmetric Zundel ions. Top frame: homogeneous countercharge distribution (—) and point charges (– – –, - - -). Center frame: static SO_3^- headgroups with full (—, – – –) and half (- - -) countercharges. Bottom frame: the case of mobile SO_3^- headgroups confined to the interface at two different proton concentrations (—, – – –) and the case of flexible side chains (- - -). Roman numbers refer to the simulations runs described in Table 1.

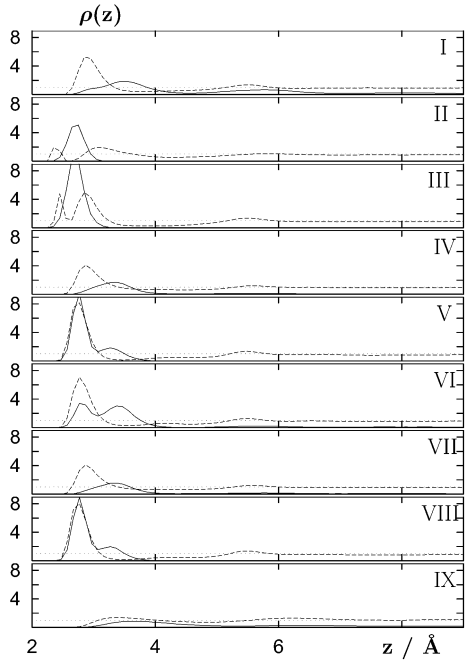

Figure 4. Density profiles of the transferring proton (—) and of oxygen atoms (– – –). A value of 1 corresponds to the density of bulk water. Proton profiles are scaled by a factor 5 for better visibility. Note the degree of localization of the protons at the surface, which is related to the overall proton mobility in the slab.

distributions for simulations II and III, in which the negative charge of the side chain is approximated by a point charge on the wall surface, are significantly different from the others. In simulations II and III, the protons stay in the Eigen state most of the time, whereas symmetric Zundel states ($q \approx 0$) are very unlikely.

In all other simulations, the distribution shows a maximum in the q region of the symmetric Zundel state and a second maximum (or at least a shoulder) for the Eigen state around $q < 0.5$ Å. Interestingly, with increasing proton concentration (or decreasing water content) (compare simulation V with IV and VIII with VII), the asymmetric proton state becomes more probable, although this behavior is not very pronounced in the case of the static sulfonate groups (runs IV and V). The shape of the distribution function of the proton-transfer coordinate is related to the proton mobility, with a larger propensity for Zundel states being indicative of faster proton diffusion (see below).

When the model allows for motion of the SO_3^- groups or for conformational fluctuations of the entire side chain, only minor changes in the distribution of the proton-transfer coordinate are observed, relative to the simulations for static SO_3^- groups (compare, for example, simulation IV with VII and V with VIII).

5.2. Density Distributions. The atom distributions in the simulated slablike laminas are best characterized by the density profiles. We define the proton location as the instantaneous position of the transferring bridge proton H_B (see Figure 2).[54] In Figure 4, the density profiles of atoms H_B are shown together with the density profiles of *all* oxygen atoms (i.e., those belonging to water molecules *and* to Zundel or Eigen complexes). The hydrogen density is scaled by a factor of 5 for better visibility.

In all simulations, there is a clear indication that the protons (solid lines) accumulate in the vicinity of the charged surfaces. In simulation I, where all direct attraction of protons to the surface is absent, this effect is entirely due to the proton−proton repulsion in the liquid phase. Modeling the Nafion phase by point charges embedded on the slab wall (simulations II and III) leads to strong localization of the protons near the countercharges.

When modeling the countercharge by extended sulfonate groups (simulations IV through VIII), we see that the localization of the protons is less pronounced. Two preferred locations are seen here—one at a distance of about 2.8 Å and one at about 3.3 Å. The precise distribution depends on the water content or, equivalently, the proton concentration (simulation IV vs V and VII vs VIII), the magnitude of the total negative countercharge (simulation VI vs IV, V, VII, and VIII), and the motion of the countercharge (IV and V vs VII and VIII) (see next section). The most important feature in simulations IV through IX is the fact that the proton distribution is wider and ranges into the second layer of water molecules. This leads to increased proton mobility (see below).

The final observation is that both for the homogeneous surface-charge simulation (I) and the most realistic simulation with completely flexible side chains (IX) the protons are less strongly localized than in the other cases. Whereas this is expected in simulation I because of the absence of localized centers for electrostatic attraction of the protons to the surface, the origin of this behavior in simulation IX is more complex. In short, any in-plane fluctuations of the positions of the SO_3^- groups smear the Coulomb barriers for the protons on the plane along the surface. We will address this issue in detail in a publication to follow.

5.3. Charge Density. A more detailed view of proton distribution near the interface can be obtained from the analysis of charge densities. Figure 5 shows proton charge-density profiles along the direction perpendicular to the slab surface

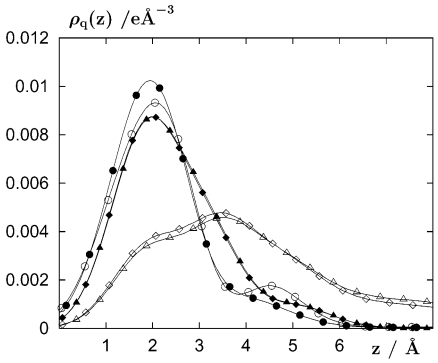

Figure 5. Charge-density profiles (for definition, see text) of the Zundel complex. Open and filled symbols are for low and high proton concentrations. Data for low proton concentration are scaled by a factor of 2. Circles are for simulations with the point-charge representation of the negative charges (simulations II and III). Diamonds and triangles are, respectively, for simulations with static (IV and V) and dynamic (VII and VIII) SO_3^- groups. Confinement of the protons near the surface is obvious for the point-charge simulations (independent of proton concentration) and for simulations with SO_3^- groups at high proton concentration. The proton distribution in simulations with SO_3^- groups at low proton concentration ranges across the entire slab.

plane. The charge density profiles $\rho_q(z)$ are obtained by a summation of the atomic charge distributions from all the atoms of the Zundel complex (to yield $\tilde{\rho}_q(z)$) and then a smoothing of $\tilde{\rho}_q(z)$ with a Gaussian of width of $\sigma = 1$ Å according to

$$\rho_q(z) = \frac{1}{\sqrt{2\pi}\sigma} \int_{\infty}^{-\infty} \exp\left[-\frac{(z'-z)^2}{2\sigma^2}\right] \tilde{\rho}(z')\, dz' \qquad (3)$$

Open and filled symbols are for low and high proton concentrations, respectively, and profiles for the low proton concentration are scaled up by a factor of 2 in order to compare the curves on the same graph.

The localization of the protons near the surface with the point-charge representation of counterions is clearly visible (circles). At the lower proton concentration (open circles), a small second maximum at around 4.5 Å from the surface is visible.

For both concentrations, the respective curves for static (diamonds) and dynamic (triangles) SO_3^- groups are very similar. Thus, the motion of the headgroup obviously does not significantly influence the average proton distribution along the z coordinate. The charge distribution is more localized for the high proton concentration than for the low concentration, in line with the theoretical expectation that the diffuse double-layer thickness near a charged surface should decrease with increasing ion concentration. Indeed, we see that in the low proton concentration ($n_w/n^+ = 27{:}1$) case, there is significant proton density even in the middle of the slab (at 11.5 Å, not shown in the Figure), whereas the proton density is practically equal to zero for the case in which $n_w/n^+ = 13.5{:}1$.

The general trend of higher proton concentration in the middle of the pore for lower total proton density is not unexpected, as the Debye screening length is larger for lower proton density. The protons are then less strongly condensed near the negatively charged surface. Some subtleties are, however, not caught by this simple mean-field consideration. We have compared the simulation results with the continuous mean-field theory[50] and auxiliary MD simulations of charged LJ spheres in a dielectric continuum. The latter were performed in the same slablike geometry as simulations IV−VIII. Both the mean-field theory and the auxiliary simulations indicate that, for a given dielectric permittivity ϵ, the density in the center of the slab should be almost independent of surface density of sulfonate groups (and thus the bulk density), at least in the concentration range investigated here. With decreasing values of ϵ, the center of the slab pore becomes more and more depleted of ions. Because of ion−ion correlations and the excluded volume (which are both present in the primitive model simulations but are not included in the simplest version of the Poisson−Boltzmann mean-field theory), the ion density decays more slowly toward the center of the pore in the quasi-primitive simulations than in the mean-field theory.

Remarkably, at the lower proton concentrations (simulations IV and VII), the ion density in the middle region of the slab is very well described by a quasi-primitive model simulation with $\epsilon = 78.5$. Simulations V and VIII at the higher proton concentrations differ from the mean-field theory and primitive model at $\epsilon = 78.5$ in two aspects: (i) because of the large polarizability of the Zundel complex, the maximum of the charge density is shifted significantly toward the surface and (ii) the density in the center is almost equal to zero, which is well reproduced in the quasi-primitive model by values of ϵ between 20 and 30. These results point toward the possibility of dielectric saturation due to the high charge density of protons and SO_3^- groups. This possible effect needs some further systematic analysis, which we postpone to a future report on double-layer effects inside PEM pores.

Figure 6 shows the charge distribution in the form of 2D proton-charge pair correlation functions $g(\rho, z)$. The negative point charges (in simulations II and III) and the sulfur positions (in the remaining simulations) are at the origin $(\rho, z) = (0, 0)$. The proton position is described as the location of the atom H_B (see Figure 2). z is the component of the counterion-charge distance perpendicular to the slab surface, and $\rho = \sqrt{x^2+y^2}$ is the component parallel to the surface plane. The bullets on the ρ axis indicate the position of the negative charges closest to the origin. For the low proton concentration runs, this position is at 9.3 Å (outside the Figure), and for the high proton concentration runs, it is at 6.6 Å. The Figure contains contour lines with values corresponding to 1 and 3 times the average density of H_B sites.

The top two frames clearly show that the point-charge model not only vertically localizes the protons near the surface but also laterally confines them into a region very close to the point charge. Other data (not shown) indicate that the oxygen atom O_1 is pinned by the point charge. Because the proton EVB state in simulations II and III is almost exclusively Eigen-like (see Figure 3), the H_B position is confined to a ring in the x, y plane that manifests itself as the two concentric contours around $(\rho, z) \approx (1, 2.8)$. The second similar feature at $(\rho, z) \approx (1, 7.5)$ and $(\rho, z) \approx (1, 6.6)$ originates from correlations between the H_B sites and the next-nearest counterion.

The two central frames show the data for the static SO_3^- groups, and the bottom frames are for the dynamic SO_3^- groups. There are significant differences between the slabs with low (left) and high (right) proton concentrations.

In the simulations at higher total proton concentration (right), the regions of proton confinement near the central charge and the closest-neighbor countercharge merge, giving rise to a broad region of high proton density for the entire ρ range (with the exception of the position immediately above the sulfur atom at $\rho \approx 0$). The protons are vertically but not laterally confined. This is fully in line with the predictions of the mean-field theory[50] because the higher-order harmonics of the electrostatic potential, responsible for the lateral variation of the electric field of the array of SO_3^- groups, die out quickly with increasing

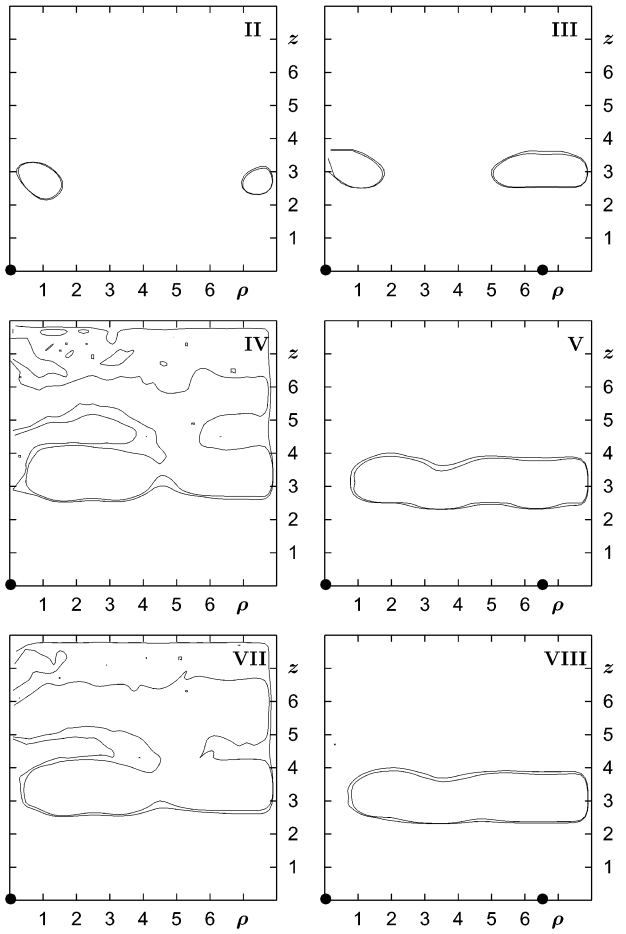

Figure 6. Contour-line representation of the 2D pair correlation function between countercharges and protons (defined as the positions of atoms H_B, see Figure 2). ρ and z are the components of the counterion−proton distance vector parallel and perpendicular to the surface, respectively. Contours are at 1 and 3 times the average proton density. Protons are confined both laterally and vertically in simulations with the point-charge representation of the countercharge (II and III). With the more realistic description of countercharges as SO_3^- ions, there is only vertical confinement at high concentration (V and VIII). At low concentration, protons fill the entire pore (IV and VII).

array density. As a consequence, the barrier for proton diffusion between the two equivalent SO_3^- sites can be expected to be rather low, thus facilitating proton transport along the surface of the slab pore.

At lower concentration, the proton distribution shifts toward the center of the slab (Figure 5). In Figure 6, this leads to a region of high proton density for a large part of the slab. Thus, at low proton concentration, a second "channel" for proton transport should open up: transport of the proton through the bulklike center of the slab. This is again fully consistent with the predictions of the mean-field theory.[49,50]

Differences of $g(\rho, z)$ between the simulations with static and dynamic SO_3^- groups are not significant. This is in line with the similarity of density (Figure 4) and charge-density profiles (Figure 5) obtained for static and dynamic SO_3^- groups.

5.4. Proton Mobility. We characterize the mobility of protons by the proton diffusion coefficients D_σ (Table 1). D_σ is not a self-diffusion coefficient but the diffusion coefficient of the proton "defect". It is calculated from the mean square displacement of the proton defect in the same way as in ref 32. The position of the proton defect is defined as the instantaneous position of the transferring proton H_B.

Table 1 contains the diffusion coefficients for 2D diffusion

$$D = \lim_{t\to\infty} \frac{\langle [x(t) - x(0)]^2 + [y(t) - y(0)]^2 \rangle}{4t} \qquad (4)$$

parallel to the slab walls, for a correlation length of 25 ps. Over the final 15 ps, the mean square displacement is a linear function of time. Error bars are estimated from the differences of diffusion coefficients in the x and y directions and from the first and second halves of the simulation.

The proton diffusion coefficients in Table 1 cover a rather large range for the selection of slab models chosen. Naturally, it is largest for the homogeneous surface-charge model (I), where there is no driving force for localization. For the point-charge model (II and III), the proton diffusion is approximately zero (smaller than the statistical error estimate); thus, the protons are completely localized or pinned. This is in line with Figure 6, which shows that the protons are both laterally and vertically confined.

The proton diffusion coefficient in bulk water at room temperature is $D = 4.7 \times 10^{-5}$ cm^2 s^{-1} for this model.[32] This value is approximately 2 times smaller than the experimental values reported in ref 53. This and the enhanced water diffusion coefficient were the main caveats of ref 32. It is, however, not the foremost purpose of this article to reproduce the absolute values but rather to understand the main trends that determine proton conductance in the membrane.

Describing the sulfonate groups as static extended four-site charge and Lennard-Jones center arrays (IV and V) increases the proton diffusion coefficient significantly. Figure 6 shows that the lateral confinement is lifted as a consequence of this more realistic description of negative charges. Furthermore, there is a substantial concentration effect that parallels the experimental trend: with increasing water content or decreasing proton concentration, the proton mobility increases (IV vs V) because of the fact that the electric double layer becomes more diffuse at the lower concentration, thereby lifting the vertical confinement. At higher water content (lower proton concentration), two possible diffusion pathways are open: one along the surface and another one through the "bulk" (see also the general discussion in section 3).

Adding sulfonate motion to the model leads to a further increase in proton mobility (compare VII with IV and VIII with V). Also, partially delocalizing the countercharge from the headgroup into the slab wall (run VI) leads to an increase in proton mobility. Finally, a realistic flexible side-chain model seems to lead to only a small additional increase in proton mobility.[55]

6. Discussion

We have simulated proton transport in a hydrophilic pore of a Nafion-type PEM by a series of increasingly realistic models. Several trends emerge:

- Proton mobility increases with increasing delocalization of the countercharge, which is distributed on the polymer side chains. With increasing charge delocalization, protons are less-strongly spatially located in the vicinity of the charge center (see Figures 4, 5, and 6). Decreasing spatial localization is related to a higher propensity for symmetric Zundel ion-like configurations of the protonic empirical valence bond state (see Figure 3). The most drastic changes are observed when changing the side-chain model from a simple point charge to a sulfonate group. These two models can be regarded as extremes of weak (point charge) and strong (sulfonate group) acids.

• Because of the electrophilic nature of the fluoride and ether oxygen ions in the Nafion side chain, part of the countercharge can be delocalized into the side chain. This is born out, for example, by the Nafion interaction potential models of Vishnyakov and Neimark,[13] which contain substantial partial negative charges on the CF_2 group and ether oxygen atoms closest to the sulfonate headgroup. In a simulation where half of the countercharge is "delocalized" into the slab surface (run VI), indeed a strong increase of proton mobility can be observed, as compared with the corresponding simulation employing full charges (run V). "Delocalizing" the entire countercharge (run I), which is equivalent to a pore confined by two homogeneously charged smooth walls, yields the highest proton diffusion coefficient of all simulated models. This limiting case corresponds to the absence of electrical work-term barriers for charge transfer;[49,50] consequently, the activation energy should be close to the one in bulk water, except for the effect of enhanced structural rigidity ("freezing") of the interfacial water layers. Of course, simulation I is not a realistic description of a PEM material such as Nafion.

• Quite expectedly, the motion of sulfonate groups leads to increased mobility of protons. The reason for this effect is probably two-fold. The first is an effective charge delocalization due to the average distribution of the sulfonate group on the surface because the sulfonate group motions smear out the Coulombic barriers that prevent protons from leaving the sulfonate group they are currently bonded to. This diminishes the activation energy of surface conductivity. Second, the increased fluctuations in electrostatical potential and mere positions of the SO_3^- groups can lead to a fluctuation-assisted reduction of the Franck−Condon barriers.

• Side-chain motion (run IX) and the associated local disorder of the charge distribution also appear to play a role in increasing proton mobility. Although this simulation is not long enough to show the effect of large conformational motions of the side chains, which occur on the time scale of several hundred picoseconds,[12] it nevertheless includes the effect of conformational disorder and librations. In this sense, mapping of the chain motions on the tethered behavior of the headgroups localized in the planes (runs VII and VIII) applies only to the fast librational motions.

In summary, we feel that the trends for proton mobility emerging from the current study can provide helpful guidelines for understanding existing membranes and for designing new membrane materials. Many open questions remain, some of which, such as the effect of differently ordered or disordered arrangements of SO_3^- groups, pore thickness, and temperature dependence, we plan to address soon. But the molecular simulations in this article already show how mechanistic features of proton transport can be rationalized by comparing the results obtained with models of different complexity.

Acknowledgment. This work has been performed as a part of the project Membranes and Membrane Electrode Assemblies for Direct Methanol Fuel Cells supported by the German government under BMWi grant 0327086. We thank the John von Neumann Institut für Computing (NIC) for generous amounts of computer time, and we acknowledge helpful discussions with A. Kuznetsov, A. Neimark, J. Ulstrup, A. Vishnyakov, and S. Walbran.

References and Notes

(1) Gottesfeld, S.; Zawodzinski, T. A. Polymer Electrolyte Fuel Cells. In *Advances in Electrochemical Science and Engineering*; edited by Alkire, R. C., Gerischer, H., Kolb, D. M., Tobias, C. W., Eds.; Wiley-VCH: Weinheim, Germany, 1997; Vol. 5, pp 195−301.

(2) 1st European PEFC Forum, July 2−6, 2001 Lucerne, Switzerland; Büchi, F. N., Scherer, G. G., Wokaun, A., Eds.; European Fuel Cell Forum: Oberrohrdorf, Switzerland, 2001.

(3) *The Fuel Cell Home*, Proceedings of the International Conference, July 2−6, 2001, Lucerne, Switzerland; Nurdin, M., Ed.; European Fuel Cell Forum: Lucerne, Switzerland, 2001.

(4) Pineri, M. In *Structure and Properties of Ionomers*; Eisenberg, A., Ed.; Reidel Publishing Co.: Dordrecht, The Netherlands, 1987.

(5) *Perfluorinated Ionomer Membranes;* Eisenberg, A., Ed.; ACS Symposium Series; American Chemical Society: Washington, DC, 1982; Vol 180.

(6) Heitner, W. C. *J. Membr. Sci*. **1996**, *120*, 1.

(7) Ise, M.; Kreuer, K. D.; Maier, J. *Solid State Ionics* **1999**, *125*, 213.

(8) Münch, W.; Kreuer, K. D.; Traub, U.; Maier, J. *J. Mol. Struct.: THEOCHEM* **1996**, *381*, 1.

(9) Paddison, S. J.; Pratt, L. R.; Zawodzinski, T.; Reagor, D. W. *Fluid Phase Equilib*. **1998**, *150−151*, 235.

(10) Paddison, S. J.; T. Z. Jr. *Solid State Ionics* **1998**, 113-115, 333.

(11) Ennari, J.; Elomaa, M.; Sundholm, F. *Polymer* **1999**, *40*, 5035.

(12) Vishnyakov, A.; Neimark, A. V. *J. Phys. Chem. B* **2000**, *104*, 4471.

(13) Vishynakov, A.; Neimark, A. V. *J. Phys. Chem. B* **2001**, *105*, 7830.

(14) Vishynakov, A.; Neimark, A. V. *J. Phys. Chem. B* **2001**, *105*, 9586.

(15) Gierer, A.; Wirtz, K. *Ann. Phys.* **1949**, *6*, 257.

(16) Agmon, N. *Chem. Phys. Lett*. **1995**, *244*, 456.

(17) Tuckerman, M.; Laasonen, K.; Sprik, M.; Parrinello, M. *J. Chem. Phys*. **1995**, *103*, 150.

(18) Tuckerman, M.; Laasonen, K.; Sprik, M.; Parrinello, M. *J. Phys. Chem*. **1995**, *99*, 5749.

(19) Tuckerman, M.; Marx, D.; Klein, M.; Parrinello, M. *Science (Washington, D.C.)* **1997**, *275*, 817.

(20) Marx, D.; Tuckerman, M. E.; Hutter, J.; Parrinello, M. *Nature (London)* **1999**, *397*, 601.

(21) Marx, D.; Tuckerman, M. E.; Parrinello, M. *J. Phys.*: *Condens. Matter* **2000**, *12*, A153.

(22) Lobaugh, J.; Voth, G. A. *J. Chem. Phys*. **1996**, *104*, 2056.

(23) Vuilleumier, R.; Borgis, D. *J. Phys. Chem. B* **1998**, *102*, 4261.

(24) Vuilleumier, R.; Borgis, D. *Chem. Phys. Lett*. **1998**, *284*, 71.

(25) Schmitt, U. W.; Voth, G. A. *J. Phys. Chem. B* **1998**, *102*, 5547.

(26) Vuilleumier, R.; Borgis, D. *J. Chem. Phys*. **1999**, *111*, 4251.

(27) Schmitt, U. W.; Voth, G. A. *J. Chem. Phys.* **1999**, *111*, 9361.

(28) Cuma, M.; Schmitt, U. W.; Voth, G. A. *Chem. Phys*. **2000**, *258*, 187.

(29) Schmitt, U. W.; Voth, G. A. *Chem. Phys. Lett*. **2000**, *329*, 36.

(30) Zahn, D.; Brickmann, J. *Isr. J. Chem*. **1999**, *39*, 469.

(31) Zahn, D.; Brickmann, J. *Chem. Phys. Lett*. **2000**, *331*, 224.

(32) Walbran, S.; Kornyshev, A. A. *J. Chem. Phys*. **2001**, *114*, 10039.

(33) Marcus, R.; Sutin, N. *Biochim. Biophys. Acta* **1985**, *811*, 265.

(34) Kuznetsov, A. M. *Charge Transfer in Physics, Chemistry and Biology: Physical Mechanisms of Elementary Processes and an Introduction to the Theory*; Gordon and Breach: Amsterdam, 1995; Chapter 6.

(35) Kuznetsov, A. M.; Ulstrup, J. *Electron Transfer in Chemistry and Biology;* Wiley: Chichester, U.K., 1999; Chapter 10.

(36) Gierke, T. D.; Munn, G. E.; Wilson, F. C. *J. Polym. Sci., Part B: Polym. Phys.* **1981**, *19*, 1687.

(37) Gebel, G.; Lambard, J. *Macromolecules* **1997**, *30*, 7914.

(38) Dreyfus, B.; Gebel, G.; Aldebert, P.; Pineri, M.; Escoubes, M.; Thomas, M. *J. Phys. (Orsay, Fr.)* **1990**, *51*, 1341.

(39) Gordeliy, V. I.; Islamov, A.; Kornyshev, A. A.; Mergel, J. To be submitted for publication.

(40) Eikerling, M.; Kharkats, Y.; Kornyshev, A. A.; Wolvkovich, Y. *J. Electrochem. Soc*. **1998**, *145*, 2684.

(41) Eigen, M.; de Maeyer, L. *Proc. R. Soc. London, Ser. A* **1958**, *247*, 505.

(42) Zundel, G.; Metzger, H. *Z. Phys. Chem*. **1968**, *58*, 225.

(43) Zundel, G.; Fritch, J. In *Spectroscopy of Solvation;* Dogonadze, R., Kalman, E., Kornyshev, A. A., Ulstrup, J., Eds.; The Chemical Physics of Solvation, Part B; Elsevier: Amsterdam, 1986; p 21.

(44) Marx, D.; Tuckerman, M. E.; Hutter, J.; Parinello, M. *Nature (London)* **1999**, *397*, 601.

(45) Schmidt, U. W.; Voth, G. A. *J. Chem. Phys*. **1999**, *111*, 9361.

(46) Kornyshev, A. A.; Kuznetsov, A. M.; Spohr, E.; Ulstrup, J. *J. Phys. Chem. B*, submitted for publication, 2002.

(47) Kornyshev, A. A.; Leikin, S.; Malinin, S. V. *Eur. Phys. J. E* **2002**, *7*, 83.

(48) Spaeth, M.; Kreuer, K.; Maier, J.; Cramer, C. *J. Solid State Chem*. **1999**, *148*, 169.

(49) Eikerling, M.; Kornyshev, A. A.; Kuznetsov, A. M.; Ulstrup, J.; Walbran, S. *J. Phys. Chem. B* **2001**, *105*, 3646.

(50) Eikerling, M.; Kornyshev, A. A. *J. Electroanal. Chem*. **2001**, *502*, 1.

(51) Mayo, S. L.; Olafson, B. D.; Goddard, W. A., III. *J. Phys. Chem*. **1990**, *94*, 8897.

(52) Berendsen, H. J. C.; Postma, J. P. M.; van Gunsteren, W. F.; DiNola, A.; Haak, J. R. *J. Chem. Phys*. **1984**, *81*, 3684.

(53) Kreuer, K.-D. In *Proton Conductors*; Colomban, P., Ed.; Cambridge University Press: Cambridge, U.K., 1992; p 474.

(54) For the symmetric Zundel ion, this definition is obvious. For the Eigen ion, the position of O_1 would be more appropriate. However, in the latter case, the average position of any of the three (equivalent) protons of the Eigen ion will be similar to the average position of O_1. For simplicity, we have thus adopted the common definition of proton position independent of proton state.

(55) The proton diffusion coefficient of simulation IX is the same as that of simulation VII within the error bars. However, the water content of simulation IX is lower than that of simulation VII. On the basis of the found dependence of the proton diffusion coefficient with water content, we would expect a higher proton diffusion coefficient if simulation IX were to be performed at the same water content as simulation VII.